



HAL
open science

Impact of axial instabilities on ion energy distribution function in Hall thruster: time-resolved RPA measurements

Quentin Delavière–Delion, F. Gaboriau, G. Fubiani, Laurent Garrigues

► **To cite this version:**

Quentin Delavière–Delion, F. Gaboriau, G. Fubiani, Laurent Garrigues. Impact of axial instabilities on ion energy distribution function in Hall thruster: time-resolved RPA measurements. 38th International Electric Propulsion Conference, Electric Rocket Propulsion Society, Jun 2024, TOULOUSE, France. pp.IEPC-2024-290. hal-04659830

HAL Id: hal-04659830

<https://hal.science/hal-04659830>

Submitted on 23 Jul 2024

HAL is a multi-disciplinary open access archive for the deposit and dissemination of scientific research documents, whether they are published or not. The documents may come from teaching and research institutions in France or abroad, or from public or private research centers.

L'archive ouverte pluridisciplinaire **HAL**, est destinée au dépôt et à la diffusion de documents scientifiques de niveau recherche, publiés ou non, émanant des établissements d'enseignement et de recherche français ou étrangers, des laboratoires publics ou privés.



Distributed under a Creative Commons Attribution - NonCommercial 4.0 International License

Impact of axial instabilities on ion energy distribution function in Hall thruster: time-resolved RPA measurements

IEPC-2024-290

Presented at the 38th International Electric Propulsion Conference
Pierre Baudis Convention Center • Toulouse, France
June 23-28, 2024

Q. Delavière--Delion¹, F. Gaboriau², G. Fubiani³ and L. Garrigues⁴
Laplace, Université de Toulouse, CNRS, INPT, Toulouse, 31062, France

Abstract: This paper presents a technique for reconstructing the temporal evolution of ion distribution functions in a Hall thruster (HT) from ion currents measured with a retarding potential analyzer (RPA). The method involves averaging discharge oscillations and temporally realigning them based on discharge current maxima. The technique was applied to ion currents from the ID-Hall 2 experimental thruster, successfully reconstructing the time-dependent ion distribution function (TIDF) in stable plasma oscillation regimes. The results indicate that deformations in the integrated ion distribution function (IDF) can be attributed to the IDF's temporal evolution over a characteristic time equal to the breathing mode oscillation period. This finding suggests potential uncoordinated displacement of ionization and acceleration zones within the discharge. However, the technique is limited in resolving higher-frequency oscillations due to their irregularity.

Nomenclature

HT	=	Hall Thruster
IDF	=	ion distribution function
$TIDF$	=	temporal ion distribution function
RPA	=	retarding potential analyser
BM	=	breathing mode
E	=	electric field
B	=	magnetic field
$ITTO$	=	ion transit time oscillation
I_d	=	discharge current
$I_{e,i}$	=	electron current balancing the extracted ion current
$I_{e,c}$	=	current of electrons crossing the magnetic barrier and coming from the cathode
V_{cg}	=	cathode potential referred to the ground
ϕ_{RPA}	=	potential of the RPA's ion filtering barrier
I_{RPA}	=	ion current collected by the RPA
m_{Xe}	=	Mass of a xenon atom in kg
e	=	elementary electric charge

¹ PhD Candidate, Université Paul Sabatier, quentin.delaviere@laplace.univ-tlse.fr.

² Associate professor, Université Paul Sabatier, freddy.gaboriau@laplace.univ-tlse.fr.

³ Senior researcher, CNRS, gwenael.fubiani@laplace.univ-tlse.fr.

⁴ Senior researcher, CNRS, garrigues@laplace.univ-tlse.fr.

I. Introduction

HALL thrusters (HT) are electric propulsion systems used for spacecraft, including orbiting satellites and exploration probes. Continuous advancements in Hall thruster technology have led to their widespread use as the primary propulsion system in geostationary satellites ¹. Despite producing lower thrust than chemical thrusters, Hall thrusters offer significantly higher specific impulse (ISP), which is proportional to the gas ejection velocity ^{2,3}.

A. Hall thruster operation

Hall thrusters, despite complex physics, operate simply: a few hundred volts DC are applied between a cathode and anode, and a radial magnetic field is imposed across the ring-shaped channel. This field traps electrons, extending their residence time and improving gas ionization. Propellant is injected and diffuses up the channel, ionizing upon collision with energetic electrons. The resulting ions are accelerated by the electric field, generating thrust, and neutralized by electrons from the cathode. The perpendicular electric and magnetic fields create a strong azimuthal electron drift current. The combination of electromagnetic fields, electron current, and plasma inhomogeneities leads to various instabilities spanning a wide range of frequencies (few Hz up to several GHz) and wavelengths (few cm to less than a mm).

B. Axial instabilities in Hall thruster

Low-pressure cross-field plasma sources, such as Hall thrusters, exhibit various instabilities that can cause oscillations ^{4,5} or turbulence ^{6,7}. Despite extensive experimental and theoretical research, the properties and nature of some instabilities remain unclear. Understanding the dynamics of these instabilities is crucial for resolving electronic transport issues across magnetic barriers.

The first type of instability in HT discharge called breathing mode (BM), is characterized by long-period, high-amplitude oscillations on discharge current ⁸, with frequencies ranging from a few kHz to tens of kHz. These oscillations have been extensively observed in experiments ⁹⁻¹⁶ and resemble a predator-prey model ¹⁷, with the frequency related to gas flow and ionization rate in the HT channel. The 1D hybrid model by Garrigues & Bœuf ¹⁸ explains this behaviour as a result of efficient ionisation depleting neutrals faster than gas flow can replace them, causing the ionization front to move towards the anode and reducing efficiency. This process leads to a cyclical pattern of virtual discharge extinction and restarting ionisation. Though more advanced models exist ^{19,20}, predicting the properties of these BM oscillations remains challenging due to interdependent mechanisms and potential interactions with other instabilities.

ITTO, occurring at frequencies from tens to hundreds of kHz, have been less studied experimentally than BM oscillations. These frequencies correspond to the inverse of ion travel time across the accelerating zone. ITTO are multi-messenger oscillations, affecting discharge current, plasma potential, electric field, and ion IDFs. They can coexist with BM oscillations but with generally lower amplitudes. Similar oscillations have been observed in fluids^{21,22}, hybrids ²³ and PIC-MMC models ²⁴. ITTO are characterised by oscillations in the potential distribution within the thruster channel, which can propagate to the plume. These oscillations affect ion acceleration, with some ions gaining additional energy by resonating on electric field waves, while others are slowed down. This results in distorted ion velocity distribution functions (IDFs), perturbed ion currents (and consequently the discharge current $I_d = I_{e,i} + I_{e,c}$), and modified ion density profiles, which in turn affect potential distribution.

This paper aims to investigate the impact of axial oscillations on mean and temporal ion velocity distribution functions. Following an introduction to our measurement test bench and the HT used, we will outline the principle of conventional retarding potential analyser (RPA) measurement. The third section presents our method for temporally resolving IDFs at frequencies of BM and ITTOs. We will then apply this method to reconstruct the time-dependent IDFs in stable oscillation regimes, discussing possible ion energy variations in relation to discharge current and capacitive signal changes. Finally, we will conclude with the suitable applications of this method.

II. Experimental set-up

A. The ID-Hall 2 thruster and vacuum testing facility

The results presented in this paper are obtained using the experimental ID-Hall 2 thruster, equipped with a MIREA-type emissive cathode ²⁵, with a constant thermic power dissipation of 240 W. This section briefly reviews the main discharge parameters. The thruster, designed at the LAPLACE laboratory, operates without an RF coil in single stage

mode (like a normal cylindrical HT). The cathode gas flow rate is maintained at 0.25 mg/s of xenon, while the thruster gas flow rates are tested between 0.6 and 0.9 mg/s. The pumping system maintains a pressure of approximately 10^{-4} mbar (10^{-2} Pa). To represent space flight conditions, the thruster's electric system is kept floating with respect to the ground, using the cathode common as the reference potential (blue wires in Fig. 1). For more information on the ID-Hall 2 thruster, please refer to the following article ²⁶.

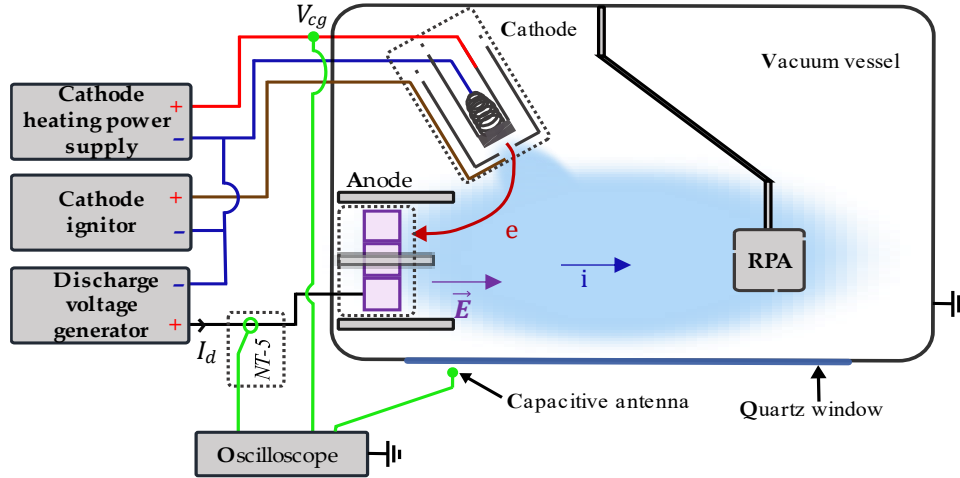


Figure 1. Thruster electrical circuit schematic diagram.

B. Diagnostics

B.1. Measurement of time varying properties

The following measurements were taken directly using a digital oscilloscope:

- The discharge current, measured between the anode and the discharge voltage generator, which produces a voltage proportional to the discharge current (green circle on Fig. 1).
- The potential difference V_{cg} between the cathode and the ground, measured at the green point on Fig. 1.
- The voltage at the electrical poles of a capacitive antenna, placed outside the chamber against the quartz side window of the vessel, capturing all electromagnetic disturbances induced by the plasma. The probe position was varied along the glass window, with no significant changes in signal shape observed below tenth of MHz.

B.2. IDF averaged over time

For measuring the mean ion distribution functions in the thruster plume, a four-grid Retarding Potential Analyser (RPA) was employed; further design details can be found in the referenced PhD thesis ²⁷. The RPA is attached to an arm that positions the screening grid 41 cm away from the thruster exit plane.

The RPA serves to filter ions based on their kinetic energy, allowing only selected ions to be detected. Utilizing four independently polarized grids (Fig. 2), the RPA functions as follows: Grid G1, the screening grid, isolates the plasma from the instrument's electric field and is left floating ($U_{G1} = V_f$). Grid G2, the electron repulsion grid, negatively polarized at $U_{G2} = -35$ V,

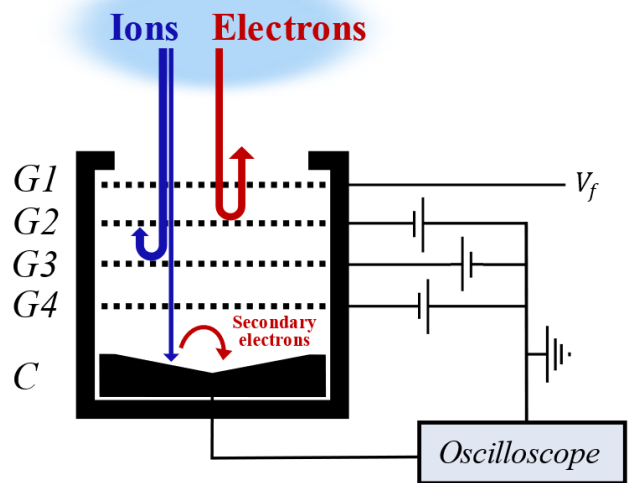


Figure 2. Sketch of the utilized retarding potential analyser and its connections.

repels electrons from the plasma, allowing only ions to pass. Grid G3, the ion discrimination/filtering grid, creates a potential barrier ϕ_{RPA} that only sufficiently energetic ions can cross, contributing to the collected current. Grid G4, another electron repulsion grid, is polarized at $U_{G4} = -40\text{ V}$ to send back secondary electrons emitted by the collector due to ion bombardment. The resulting collector current I_{RPA} , induced by ions impacting the collector C, is proportional to the ion charge flux entering the RPA with energy greater than the minimum required to cross the barrier $J_{RPA}(\phi_{RPA}) = J_{RPA}(v_{min})$, and can be measured using an oscilloscope.

$$I_{RPA} = J_{RPA}(v_{min}) S_{RPA} \tau_{tr} \quad (1)$$

$$J_{RPA}(v_{min}) = q_i e n_i \int_{v_{min}}^{+\infty} v f(v) dv \quad (2)$$

With $v_{min} = \sqrt{\frac{2 q_i e \phi_{RPA}}{m_i}}$ the minimum velocity required to cross the potential barrier ϕ_{RPA} , S_{RPA} is the surface area of the RPA collection zone and τ_{tr} its transparency; these two parameters are unknown to us. The mass of the ion is noted m_i , its charge number q_i and e the elementary charge. We note f the ion velocity distribution function (IVDF):

$$f(\phi_{RPA}) = -\frac{1}{S_{RPA} \tau_{tr} q_i^2 e^2} \frac{m_i}{d\phi_{RPA}} \frac{dI_{RPA}(\phi_{RPA})}{d\phi_{RPA}} \quad (3)$$

$$f(\phi_{RPA}) \propto -\frac{dI_{RPA}(\phi_{RPA})}{d\phi_{RPA}} \quad (4)$$

It is important to clarify that the IVDF is directly proportional to the derivative of the collected current with respect to the potential applied to the RPA. In this context, we are discussing an Ion Velocity Distribution Function (IVDF), not an Ion Energy Distribution Function (IEDF). The confusion often arises due to the conventional use of energy units (eV) to express velocities. The IEDF g is given by the following formula, where energy is represented by E :

$$g(E) = f(v) \frac{1}{m_i v} \quad (5)$$

An additional correction is required to account for the potential difference between the floating electrical system of the thruster and the ground-referenced RPA. This is done by subtracting $q_i V_{cg}$ from the measured ion energy, where $q_i = 1$ (considering only singly charged ions).

In practice, a voltage ramp is applied to the discriminator grid using a voltage generator controlled by a function generator, which provides a triangular reference signal with chosen frequency and amplitude. The voltage ramp extremes are selected to cover the variation zone of the IDF for each operating condition. The frequency of the voltage ramp is set at 0.5 Hz, much lower than plasma oscillation frequencies, to average out any potential impacts from these oscillations in the collected signal. The oscilloscope measures both the current from the RPA collector and the voltage applied to the filter grid. To reduce noise, each measurement series is averaged over 16 cycles on the oscilloscope. Before calculating the IDF, the measured signals are filtered using the Stavisky-Golay^{28,29} algorithm to minimize noise that could be amplified by the derivative calculation in equation (4). The obtained IDFs are then further processed by the SG algorithm for final filtering.

III. Time-resolved IDF reconstruction

The time averaging principle in the previous RPA method does not enable the probing of potential changes in the IDF during the characteristic instability times. The target low-frequency oscillations in the Hall discharge have frequencies ranging from a few kHz to MHz, whereas the ion population measurements are taken at a much lower frequency of 0.5 Hz.

A. Data acquisition

To capture the IDF dynamics during various oscillations, one might consider increasing the voltage ramp frequency. However, generating a complete I/V trace at the Nyquist frequency of the oscillation is challenging due to the limited availability of variable voltage generators capable of sweeping 300 V at several hundred kHz and the issue of capacitive effects inside the instrument. An alternative and simpler technique is to set a constant filter potential on the filter grid, $\phi_{RPA,m}$, and record the time series of the collected current, $I_{RPA}(t, \phi_{RPA,m})$, for this voltage. The filter voltage is then changed to $\phi_{RPA,n}$, and the acquisition of $I_{RPA}(t, \phi_{RPA,n})$ is repeated until the entire area of interest is scanned, which is determined by studying the average IDF.

During acquisitions, the potential associated with the discharge current, the capacitive potential of an antenna outside the vacuum vessel, the current collected by the RPA, and the cathode potential relative to ground are recorded simultaneously on a digital oscilloscope. To avoid low-pass filtering by the oscilloscope, a current-voltage converter Hamamatsu C12419 combined with a broadband amplifier is used to measure ions currents. To minimize measurement noise, regardless of the data processing technique used, it is common and more practical to average the signals directly on the oscilloscope. Thus, the acquisitions were obtained by averaging the signals over 16 times.

B. Data pre-processing

The temporal IDFs are reconstructed from the different time series of current as a function of potential V_m . Several data processing procedures exist, including FFT³⁰, time realignment¹³, discharge forcing³¹, empirical transfer function³², and shadow manifold interpolation³². All these methods require highly reproducible and perfectly periodic plasma oscillations, as any instability in the central frequencies could significantly affect the reconstructed IDF quality. Although temporal IVDF measurements have been conducted using LIF (laser induced fluorescence)^{33,34}, few temporal measurements at the RPA are found in the literature^{13,30,35,36}. We chose to use a time realignment technique based on a reference signal, which must be periodic, representative of the discharge, and unaffected by RPA setting changes. The discharge current was chosen as the indicator, but the capacitive signal could also be used.

Before aligning the data, it is important to verify the measurement validity. One way is to compare the collected currents using the integrated method (traditional RPA use) and the time-averaged method at a series of fixed filter voltages. This involves averaging each time series $I_{RPA}(t, \phi_{RPA})$ over time to obtain $\overline{I_{RPA}}(\phi_{RPA})$, which is then compared with the time-integrated current measurement $I_{RPA}(\phi_{RPA})$. The top graph of Fig. 3 shows this comparison, revealing that while the trends seem similar, the current values differ: the integrated current is consistently greater than the time-averaged current. The differences can be attributed to the oscilloscope's averaging function during signal acquisition: while this technique reduces noise, it also dampens oscillations that are not perfectly periodic. Consequently, the mean value of the signal is better estimated, but the signal amplitude decreases more rapidly when calculated over many samples with irregular oscillation frequencies, as shown in Fig. 4. In relatively stable discharges, the change in BM frequency causes a loss of approximately 1/3 of the total amplitude over 3 periods, whereas in more irregular discharges, this instability results in the loss of almost half the signal amplitude over 3 periods. To achieve quality results, it is crucial to stay close to the original triggering time, within the green transparency zone. This phenomenon is an artifact caused by the combination of averaging and the irregularity of the central frequencies of different oscillations, along with the impact of the oscilloscope's trigger threshold effects, explaining why oscillations centred on time zero are the most similar.

It is possible to calculate the IDF associated with the currents $I_{RPA}(\phi_{RPA})$ and $\overline{I_{RPA}}(\phi_{RPA})$ shown in Fig. 3 using Eq. (4). The resulting IDF graphs can be seen in Fig. 5. They are very similar, although there are slight differences between the distribution functions. These discrepancies can be attributed to a combination of factors, such as different sampling steps between the integrated and time measurements, leading to a slight offset when calculating derivatives.

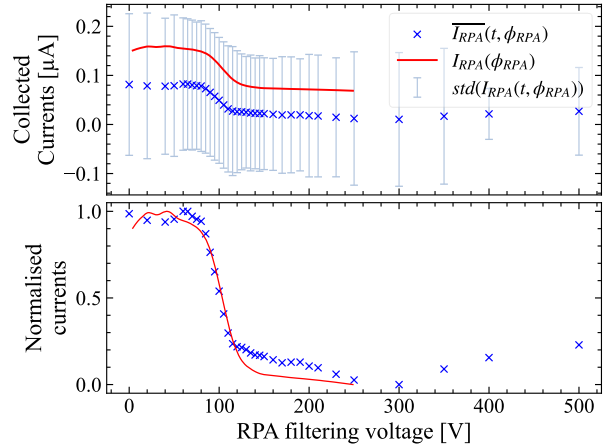


Figure 3. Comparison of the collected currents using the RPA with a voltage ramp (red solid curve) and by averaging the time series for each filter voltage (blue crosses). Top graph: direct current comparison. Bottom graph: current comparison after normalization by an affine function. ID-Hall 2 with 0.9 mg/s of xenon at $U_d = 120V$.

Additionally, the thruster's behaviour experienced a slight deviation over dozens of hours of firing. Nevertheless, the differences are small enough to consider the dataset usable.

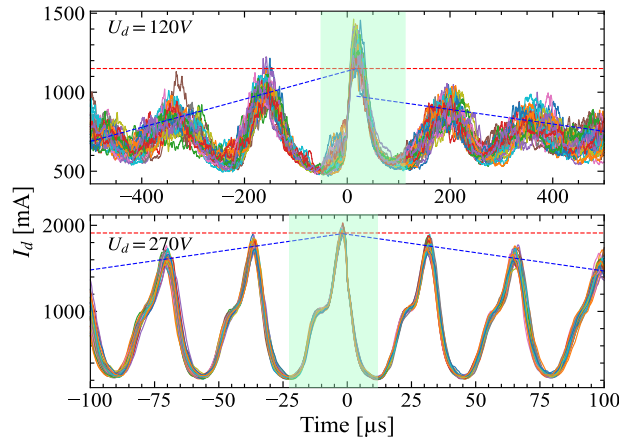


Figure 4. Discharge currents averaged over 16 cycles by the oscilloscope for a gas flow rate of 0.9 mg/s of xenon and discharge voltages of 120V (top) and 270V (bottom). Each signal corresponds to a different RPA filter voltage.

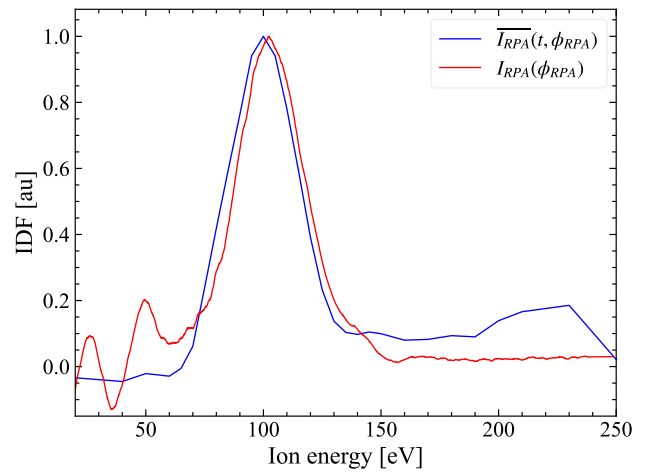


Figure 5. Comparison of IDF obtained by direct derivation of RPA current as a function of retarding potential (red curve) and from time series averaging (blue curve).

C. Data processing

To reduce noise in the signals, the first step is to filter the time-series data. To achieve maximum noise reduction, the data was oversampled during acquisition. For filtering procedures, the chosen method is filtering in Fourier space, in which all oscillations with frequencies above the selected cut-off frequency f_c are eliminated $f_c = 1$ MHz.

The objective of the subsequent steps is to synchronize the various time series to reconstruct the currents based on the RPA filter voltage and a common time. As only the RPA barrier potential is altered in each time series, the thruster discharge current is deemed perfectly reproducible and thus employed as the time reference to synchronize the time series (using the capacitive signal instead of discharge current yield to identical results).

The protocol reconstructs time series by identifying a reference time in the discharge current for each series, using the maximum current on the BM oscillation closest to the measurement time origin. To detect the most significant peak, a local maxima search algorithm based on relative amplitude and oscillation prominence is employed. Once the maximum position $t_{Id,max}$ is measured, the time series retains only points within the interval $[t_{Id,max} - T_{BM}/2, t_{Id,max} + T_{BM}/2]$, where T_{BM} is the BM oscillation period. This process is repeated for all series. The realignment can be quickly verified by superimposing the discharge currents. As we can see in Fig. 6, the alignment is not perfect due to non-periodic discharge oscillations, making the method unsuitable for excessively irregular conditions.

For improved clarity, Fig. 7 displays a 2D map of the ion current reaching the RPA collector as a function of a common time and the energy required to cross the potential barrier. The time origin corresponds to the moment when the discharge current reaches its maximum during a BM cycle. To generate the map in Fig. 7, an additional step was required: like obtaining the average IDF by voltage ramp, the difference

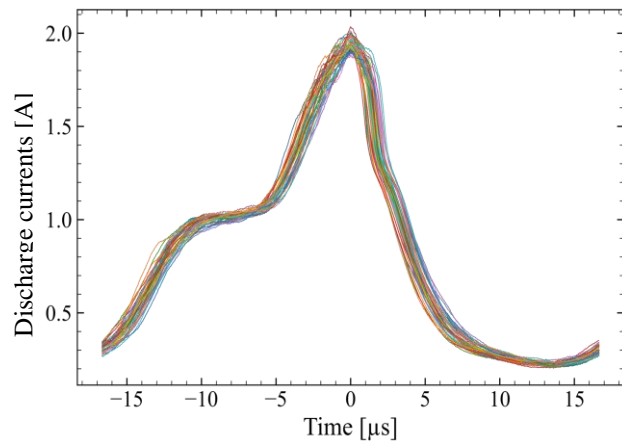


Figure 6. Superimposed discharge currents for a fixed discharge voltage of 270 V.

between the cathode potential and the ground must be subtracted from the RPA's filter voltage to obtain the actual ion energy. A continuous and intense band is observed across the energy domain at times -1, 4, and 6 μs . It is unlikely that a significant number of ions are accelerated to energies exceeding 450 eV with $U_d = 270\text{ V}$; thus, this phenomenon can be attributed to capacitive effects on the RPA and its acquisition line, possibly due to fluctuations in plasma potential. Assuming these capacitive effects are independent of the probed ion energy and periodic in time for fixed discharge conditions, the mean of currents measured beyond a hundred volts above the discharge voltage is subtracted from the current ensemble for each time. This involves subtracting ion currents collected with RPA potential barrier settings between 370 and 500 V for a discharge voltage of 270 V, resulting in the new current map shown in Fig. 8.

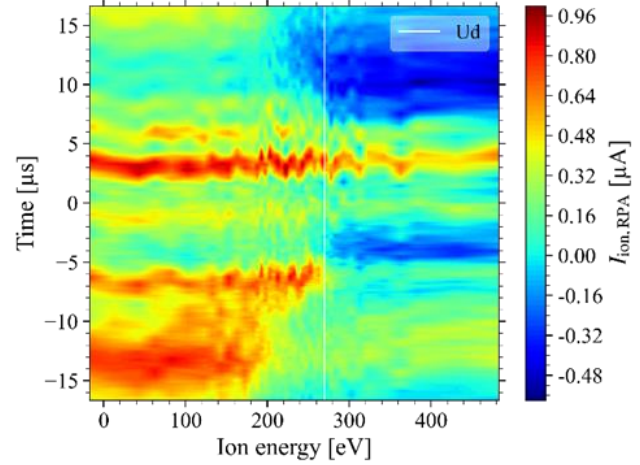


Figure 7. Map of ion current collected by the RPA as a function of the potential applied to the discriminator grid at a fixed discharge voltage of 270 V.

To obtain the IDF as a function of time, the collected ion current is differentiated along the energy axis according to equation (4). Before performing this final operation, currents are filtered along the energy axis to eliminate strong fluctuations caused by discharge irregularities over time. The result is a graph of $IDF(t, E_k)$ shown in Fig. 9, which displays the evolution of the ion energy distribution during a BM period.

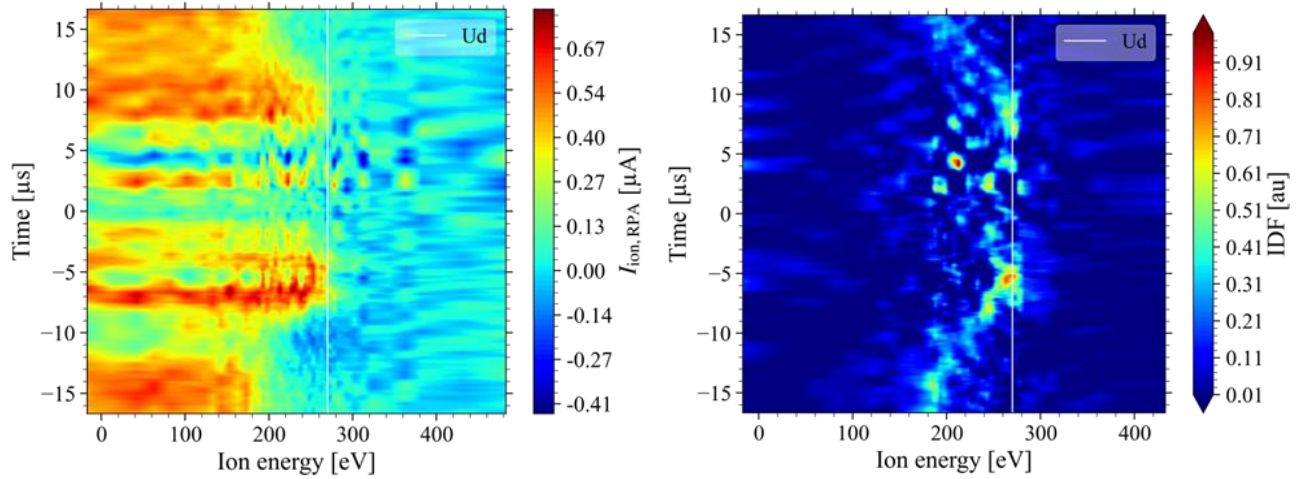


Figure 8. Map of the ion current collected by the RPA corrected for capacitive effects. Figure 9. IDF(t, E_k) 2D map for $U_d = 270\text{V}$.

To facilitate comparison with other measured quantities, IDFs were corrected for distortions due to ions' time of flight to the RPA. Assuming that ions are no longer accelerated beyond the thruster exit plane, IDFs were reconstructed at the thruster exit plane using equations (7) and (8). For each current defined by collection time and minimum energy, IDF time axis alignment was calculated considering t_{RPA} (signal pickup time), $t_{exit\ plane}$ (ion emission time), $\Delta t_{flight\ time}$ (ion time of flight), and $d_{RPA-exit\ plane}$ (distance between thruster outlet plane and RPA manifold). This implies that each energy level should be shifted by a time equivalent to the time required for ions to reach the RPA, with more energetic ions having shorter travel times. The resulting transformation is displayed in Fig. 10.

$$t_{exit\ plane} = t_{RPA} - \Delta t_{flight\ time} \quad (7)$$

$$\Delta t_{flight\ time} = d_{RPA-exit\ plane} \sqrt{\frac{m_{Xe}}{2e(\phi_{RPA} - V_{cg})}} \quad (8)$$

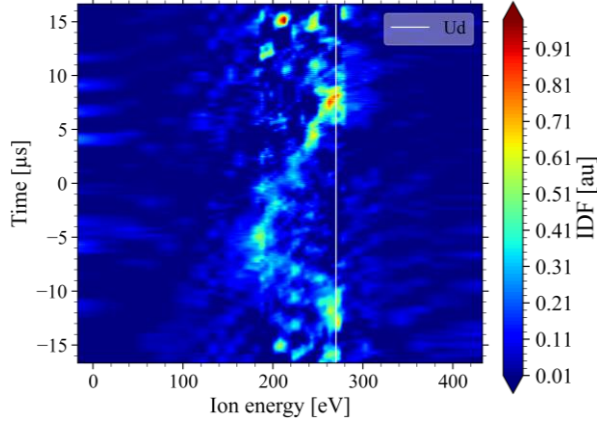


Figure 10. IDF(t, E_k) 2D map for $U_d = 270V$ at the exit plane level of the Hall thruster.

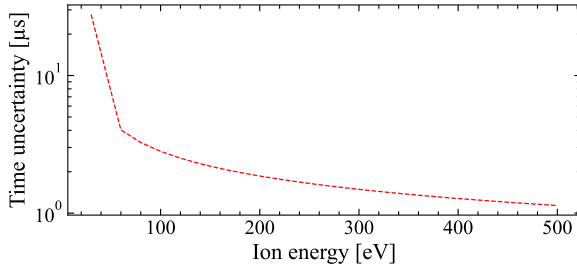


Figure 11. Overall time shift uncertainty

There are multiple sources of uncertainty in ion energy:

- The uncertainty in the voltage supplied by the generator and applied to the filter grid is 0.5 V.
- Fluctuations in the cathode coupling potential relative to ground have maximum amplitudes of 3 V, but the RPA measurement step is at least 5 V in ion current variation areas. These fluctuations cannot be corrected and are masked by voltage sampling resolution.
- Potential drop loss in the electrostatic sheath at the RPA input. Assuming plasma potential variations are transmitted with the same amplitude and phase at the sheath output, floating potential variations equal plasma potential variations, with only their average values differing. This hypothesis is verified for fluctuations below 1 MHz³⁷.

The ion energy uncertainty is estimated at around 5 eV. This uncertainty affects only the absolute energy value and not the time position of energies in Fig. 7-10.

The uncertainty in the time adjustment is determined by considering the uncertainty in the distance between the RPA collector and the ion extraction zone, as well as the ions' speed. This uncertainty depends on the ions' energy and is presented in the graph in Fig. 11. It is calculated by computing the time of flight over the uncertain distance for an ion with a kinetic energy ranging from 1 to 500 eV. In the IDF variation zone (between 200 and 300 V), the uncertainty ranges from 2 to 1.5 μs .

IV. Results & discussion

A. Oscillation regime in ID-Hall 2 plasma

Several oscillation regimes have been identified:

- Regime A: Low-frequency BM oscillation for discharge voltage $U_d \in [105-175]$ V.
- Regime B: High-frequency and high-amplitude BM oscillation for $U_d \in [175-335]$ V.
- Regime C: Unstable BM oscillation for $U_d \in [335-408]$ V, with significant electronic current increase through the anode.

BM oscillations are present at least transiently in all regimes, accompanied by fast oscillations with lower amplitudes and frequencies of several tens to hundreds of kHz during the maximum discharge current phase. Each rapid discharge current oscillation corresponds to a signal peak on the external capacitive antenna, suggesting a correlation between ion current variations (potentially causing increased discharge current) and electric field reorganization in the plasma. This observation supports the interpretation of these rapid oscillations as Ion Transit Time Oscillations (ITTOs). A comprehensive study of oscillation regimes has been conducted, with results available in this reference²⁷. In regime B, oscillations in the hundreds of kHz overlap with certain BM harmonic frequencies. Additionally, the amplitude of discharge current oscillations doubles in this regime, suggesting a potential resonating interaction between the two oscillations.

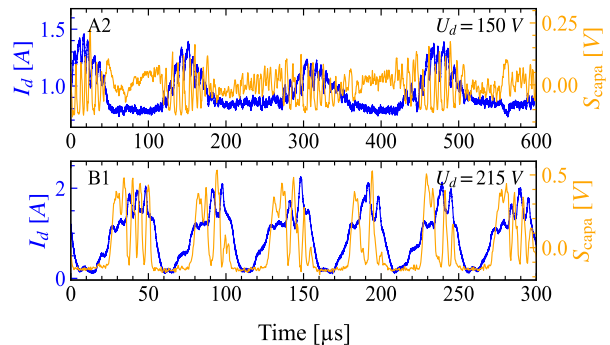


Figure 12. A time series examples in A and B regimes, with the I_d shown in blue and the external capacitive antenna voltage in orange.

B. Temporal ion distribution function

Following the data collection and processing protocols established in section III, the temporal evolution of the IDF was reconstructed. Fig. 14 shows, for one discharge voltage (from left to right), the map of ion current collected by the RPA as a function of time and potential applied to the discriminator grid, the 2D IDF map as a function of time during one BM cycle (calculated in the thruster exit plane), and some IDF snapshots for fixed times.

The discharge voltage is fixed to $U_d = 270V$, in regime B. The integrated IDF is significantly distorted with a considerable proportion of fast ions, resulting in distribution asymmetry. On the ion current map, both the maximum energy reached and the ion current value increase between -15 and $-5 \mu s$. This change is reflected in the IDF map: initially, ion energy collapses before the BM starts its rising phase (before $-20 \mu s$). As the discharge current begins to increase, ion energy stabilizes around $170 eV$. A plateau in the discharge current follows, during which a pulse is captured on the capacitive signal, and the IDF shifts towards higher energies ($205 eV$). During the discharge current's resumption of growth, the IDF's translation slows down and stabilizes at a maximum when I_d is maximum ($270 eV$). During the BM's descending phase, the ion current is insufficient for accurate IDF determination. The integrated IDFs obtained through both methods are very similar.

The key observation is that in regime B, during a BM cycle, the ion energy is relatively low and constant when the discharge current first increases. When the current plateau on I_d is reached, the average ion energy starts to increase, coinciding with a pulse captured on the capacitive antenna. This pulse likely represents the electric field variation responsible for ion acceleration, suggesting the presence of ITTO. When I_d reaches its maximum and all gas atoms are ionized, the current rapidly decreases, and the IDF is lost due to weak or irregular ion current.

A significant limitation of our diagnosis is the oscillations irregularity, requiring signal averaging during acquisition. This averaging affects signal shapes, such as observing only one rapid oscillation superimposed on the BM in the $U_d = 270V$ discharge current of Fig. 14, compared to 2-3 oscillations in Fig. 12. The ion response is also averaged, highlighting a single variation in the ion's average energy as if the phenomenon were continuous. However, simulations with visible ITTO on the BM show as many IDF energy alternations as oscillations on the BM¹⁷. To verify if our reconstruction algorithm can probe IDFs at frequencies around hundreds of kHz, it was tested on time series from simulations presented in article¹⁷. Each visible BM on the collected ion currents was averaged to simulate current acquisition by the RPA and oscilloscope. Our algorithm's results matched those obtained by directly counting particles in the model, confirming that the ion distributions were achievable with the desired time resolution, even with slight discharge variability. So, simulations suggest that ITTO oscillations in discharge currents would be reflected in ion energy distribution functions as variations in ion energy at ITTO frequencies. However, these variations are not observed in our data due to the necessary averaging of discharge oscillations to obtain the most reproducible current shape. As ITTO oscillations are more random than BM oscillations, they are lost in the averaging process.

To experimentally solve IDFs at ITTO frequencies, it is necessary to eliminate the averaging operation. One approach could be to identify similar oscillation patterns in each time series associated with potential RPA filtering over a large time period. By assuming that similar effects produce similar consequences for ion movements at ITTO frequencies, IDFs could be reconstructed for an oscillation typology that includes both BM and ITTOs.

Currently, we can assume that during a BM oscillation, ionization and acceleration zones move independently, altering the total electric field seen by an ion at a given location and time. Recent hybrid code simulations suggest that an axial displacement of the ionization zone in the BM (at the BM frequency) can generate a TIDF modification like that observed in regime B in Fig. 14. Additionally, ITTOs may destabilize the BM, causing its electric field to move or deform, allowing ions to gain more speed and potentially transferring kinetic energy from some ions to accelerate others, resulting in super-energetic ions.

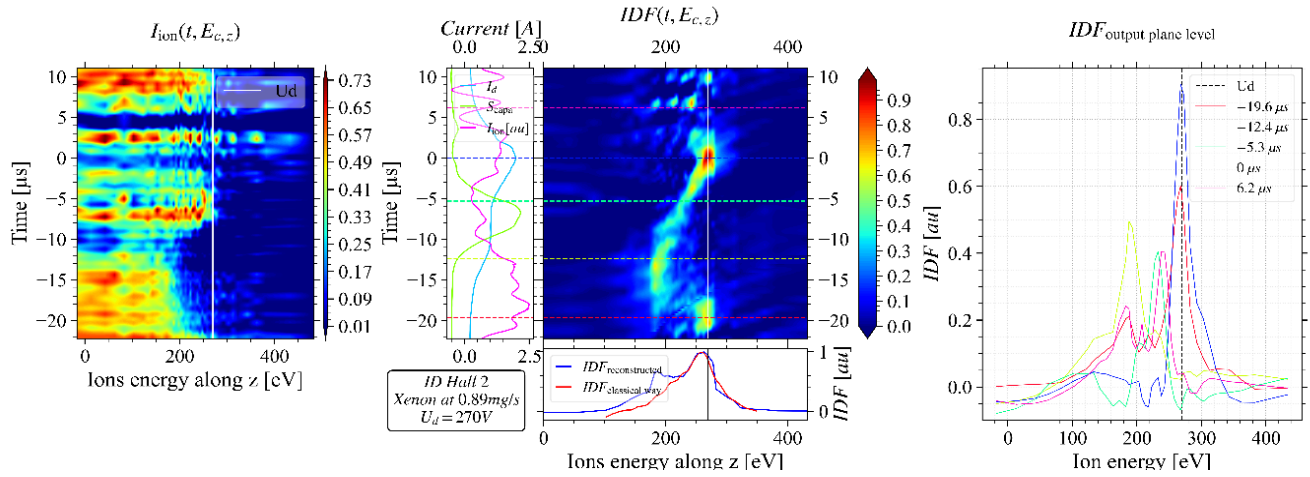


Figure 14. The left graph shows the current collected by the RPA as a function of the voltage applied to the RPA discriminator grid, corrected for the cathode potential. The middle graph displays the $IDF(E_{c,ion}, t)$ map, while the lower graph compares the IDF obtained from RPA measurements with a voltage ramp (red) and the calculated averaged $IDF(E_{c,ion})$ (blue), sharing the energy axis with the main graph. The left-hand side graph shows discharge currents, reconstructed ion current, and capacitive signal. The time axis is shared between the central graph and the left-hand side graph, with a time shift applied to correct the time-of-flight IDF. Colored dotted lines mark selected times for detailed analysis on the right-hand graph. The right-hand side graph shows IDFs for selected times during a BM cycle for a discharge voltage of 270V and 0.9 mg/s xenon.

I. Conclusion

In this study, a technique inspired by Langmuir probe time measurements was adapted to RPA ion current measurements to reconstruct ion distribution functions (IDFs) over time, on the scale of ITTO and BM oscillations. Applying this algorithm to ion currents collected in each previously identified regime helped explain the different shapes of integrated classical IDFs in these regimes. However, the discharge's irregularity did not enable IDF resolution on the ITTO scale. Nevertheless, when the discharge was sufficiently periodic, a modulation of the energy acquired by the ions at the BM oscillation frequency was observed, suggesting a possible decoupling of ionization and acceleration zones. Depending on the ion creation time and location, the perceived accelerating electric field varied, with distribution and overlap between these zones evolving with BM instability.

Acknowledgments

Q. DD has benefited from a PhD funding from the French Ministry of Research. This work is supported by the CNES agency.

This work has been carried out within the framework of the EUROfusion Consortium, funded by the European Union via the Euratom Research and Training Programme (Grant Agreement No 101052200—EUROfusion). Views and opinions expressed are however those of the author(s) only and do not necessarily reflect those of the European Union or the European Commission. Neither the European Union nor the European Commission can be held responsible for them.

References

- ¹ D. Lev, R.M. Myers, K.M. Lemmer, J. Kolbeck, H. Koizumi, and K. Polzin, "The technological and commercial expansion of electric propulsion," *Acta Astronautica* **159**, 213–227 (2019).
- ² S. Mazouffre, "Electric propulsion for satellites and spacecraft: established technologies and novel approaches," *Plasma Sources Sci. Technol.* **25**(3), 033002 (2016).
- ³ D. Krejci, and P. Lozano, "Space Propulsion Technology for Small Spacecraft," *Proc. IEEE* **106**(3), 362–378 (2018).
- ⁴ E.Y. Choueiri, "Plasma oscillations in Hall thrusters," *Phys. Plasmas* **8**(4), 1411 (2001).
- ⁵ V. Mazières, F. Gaboriau, A. Guglielmi, V. Laquerbe, R. Pascaud, and O. Pascal, "Broadband (kHz–GHz) characterization of instabilities in Hall thruster inside a metallic vacuum chamber," *Phys. Plasmas* **29**(7), 072107 (2022).
- ⁶ S. Tsikata, A. Héron, and C. Honoré, "Hall thruster microturbulence under conditions of modified electron wall emission," *Phys. Plasmas* **24**(5), 053519 (2017).
- ⁷ Yamamoto, Kuwabara, Cho, Kosuga, and Dif Pradalier, "Observation of Plasma Turbulence in a Hall Thruster Using Microwave Interferometry," *J. Propul. Power*, (2023).

- ⁸ A. Guglielmi, Propulseur à courant de Hall double étage à source RF inductive: étude expérimentale du fonctionnement et des instabilités basses fréquences, PhD thesis, Paul Sabatier, 2020.
- ⁹ E. Chesta, C.M. Lam, N.B. Meezan, D.P. Schmidt, and M.A. Cappelli, "A characterization of plasma fluctuations within a Hall discharge," *IEEE Trans. Plasma Sci.* **29**(4), 582–591 (2001).
- ¹⁰ J. Kurzyna, S. Mazouffre, A. Lazurenko, L. Albarède, G. Bonhomme, K. Makowski, M. Dudeck, and Z. Peradzyński, "Spectral analysis of Hall-effect thruster plasma oscillations based on the empirical mode decomposition," *Phys. Plasmas* **12**(12), 123506 (2005).
- ¹¹ L.-Q. Wei, L. Han, D.-R. Yu, and N. Guo, "Low-frequency oscillations in Hall thrusters," *Chinese Phys. B* **24**(5), 055201 (2015).
- ¹² K. Hara, S. Keller, and Y. Raitses, "Measurements and theory of driven breathing oscillations in a Hall effect thruster," in *52nd AIAA/SAE/ASEE Joint Propulsion Conference*, (American Institute of Aeronautics and Astronautics, Salt Lake City, UT, USA, 2016).
- ¹³ A. Guglielmi, A. Martín Ortega, F. Gaboriau, and J.-P. Boeuf, "Influence of double-stage operation on breathing oscillations and rotating spokes in the ID-HALL thruster," in *36th International Electric Propulsion Conference*, (Vienne, Autriche, 2019).
- ¹⁴ A. Martín Ortega, A. Guglielmi, F. Gaboriau, C. Boniface, and J.P. Boeuf, "Experimental characterization of ID-Hall, a double stage Hall thruster with an inductive ionization stage," *Phys. Plasmas* **27**(2), 023518 (2020).
- ¹⁵ V. Giannetti, M.M. Saravia, and T. Andreussi, "Measurement of the breathing mode oscillations in Hall thruster plasmas with a fast-diving triple Langmuir probe," *Phys. Plasmas* **27**(12), 123502 (2020).
- ¹⁶ M. Baird, T. Kerber, R. McGee-Sinclair, and K. Lemmer, "Plume Divergence and Discharge Oscillations of an Accessible Low-Power Hall Effect Thruster," *Appl. Sci.* **11**(4), 1973 (2021).
- ¹⁷ J. Bareilles, G.J.M. Hagelaar, L. Garrigues, C. Boniface, J.P. Boeuf, and N. Gascon, "Critical assessment of a two-dimensional hybrid Hall thruster model: Comparisons with experiments," *Phys. Plasmas* **11**(6), 3035–3046 (2004).
- ¹⁸ J.P. Boeuf, and L. Garrigues, "Low frequency oscillations in a stationary plasma thruster," *J. Appl. Phys.* **84**(7), 3541–3554 (1998).
- ¹⁹ T. Lafleur, P. Chabert, and A. Bourdon, "The origin of the breathing mode in Hall thrusters and its stabilization," *J. Appl. Phys.* **130**(5), 053305 (2021).
- ²⁰ O. Chapurin, A. Smolyakov, G. Hagelaar, J.-P. Boeuf, and Y. Raitses, "Fluid and hybrid simulations of the ionization instabilities in Hall thruster," *J. Appl. Phys.* **132**(5), 053301 (2022).
- ²¹ J. Vaudolon, and S. Mazouffre, "Observation of high-frequency ion instabilities in a cross-field plasma," *Plasma Sources Sci. Technol.* **24**(3), 032003 (2015).
- ²² J. Vaudolon, Electric Field Determination and Magnetic Topology Optimization in Hall Thruster, PhD thesis, ICARE - Institut de Combustion, Aérothermique, Réactivité et Environnement, 2015.
- ²³ G.J.M. Hagelaar, J. Bareilles, L. Garrigues, and J.-P. Boeuf, "Two-dimensional model of a stationary plasma thruster," *J. Appl. Phys.* **91**(9), 5592–5598 (2002).
- ²⁴ F. Petronio, Plasma Instabilities in Hall Thrusters: A Theoretical and Numerical Study, PhD thesis, École Polytechnique, 2023.
- ²⁵ A. Loyal, F. Daron, L. Albarede, V. Lago, P. Lasgorceix, and M. Dudeck, "Correlation Between Hollow Cathode Operating Conditions and Hall Thruster (SPT100-ML) Performance Characteristics," in *38th AIAA/ASME/SAE/ASEE Joint Propulsion Conference & Exhibit*, (American Institute of Aeronautics and Astronautics, Indianapolis, Indiana, 2002).
- ²⁶ Q. Delavière--Delion, F. Gaboriau, G. Fubiani, and L. Garrigues, "Experimental observation of low-frequency interactions at different scales and evidence of transit time oscillations in a Hall thruster: Spectral analysis," Submitted for Publication, (2024).
- ²⁷ C. Philippe Kadlec, Caractérisations spatio-temporelles de jets ioniques : développement des diagnostics et application a la propulsion ionique, PhD thesis, GREMI, 1998.
- ²⁸ H. Andrei, V. Covlea, V.V. Covlea, and E. Barna, "The smoothing and the digital processing of Langmuir probe characteristic," *Romanian J. Phys.* **55**(2), 51–56 (2003).
- ²⁹ A. Caldarelli, F. Filleul, R.W. Boswell, C. Charles, N.J. Rattenbury, and J.E. Cater, "Data processing techniques for ion and electron-energy distribution functions," *Phys. Plasmas* **30**(4), 040501 (2023).
- ³⁰ M. Baird, T. Kerber, K. Lemmer, and W. Huang, "Hall Thruster Plume Measurements of Time Resolved Ion Energy," in *36th International Electric Propulsion Conference*, (University of Vienna, Austria, 2019).
- ³¹ I. Romadanov, Y. Raitses, A. Diallo, I.D. Kaganovich, K. Hara, and A. Smolyakov, "Time-resolved measurements of modulated breathing oscillations in cylindrical Hall Thruster," in *35th International Electric Propulsion Conference*, (Georgia Institute of Technology • Atlanta, Georgia • USA, 2017).
- ³² A. Thomas, and K. Lemmer, "Time-resolved ion energy measurements using a retarding potential analyzer for electric propulsion applications," *Rev. Sci. Instrum.* **95**(2), 023505 (2024).
- ³³ V.H. Chaplin, R.B. Lobbia, A. Lopez Ortega, I.G. Mikellides, R.R. Hofer, J.E. Polk, and A.J. Friss, "Time-resolved ion velocity measurements in a high-power Hall thruster using laser-induced fluorescence with transfer function averaging," *Appl. Phys. Lett.* **116**(23), 234107 (2020).
- ³⁴ A. Lucca Fabris, C.V. Young, and M.A. Cappelli, "Time-resolved laser-induced fluorescence measurement of ion and neutral dynamics in a Hall thruster during ionization oscillations," *J. Appl. Phys.* **118**(23), 233301 (2015).
- ³⁵ M. Baird, R. McGee-Sinclair, K. Lemmer, and W. Huang, "Time-resolved ion energy measurements using a retarding potential analyzer," *Rev. Sci. Instrum.* **92**(7), 073306 (2021).
- ³⁶ T. Gibert, L. Balika, F. Diop, and A. Bouchoule, "Doubly-Charged Xe Ions Evidenced by Time Resolved RPA Measurement in the Far Field Plume of a Low-Power HET," *Contrib. Plasma Phys.* **55**(7), 529–537 (2015).
- ³⁷ J.F. Caneses, and B. Blackwell, "RF compensation of double Langmuir probes: modelling and experiment," *Plasma Sources Sci. Technol.* **24**(3), 035024 (2015).